Appl. Phys. A 86, 451–456 (2007)
DOI: 10.1007/s00339-006-3806-7

Applied Physics A
Materials Science & Processing

P. LEMOINE✉
S.S. ROY
J.P. QUINN
P.D. MAGUIRE
J.A.D. MCLAUGHLIN

Carbon nanostructures grown with electron and ion beam methods

The Nanotechnology and Integrated BioEngineering Centre, University of Ulster at Jordanstown, Newtownabbey, Co. Antrim BT37 0QB, Northern Ireland, UK

Received: 31 July 2006/Accepted: 21 November 2006
Published online: 13 January 2007 • © Springer-Verlag 2007

ABSTRACT We present a comparative study where carbon nanostructures were prepared by electron and ion beam methods. Thin films of $10 \times 10\,\mu m^2$ area were prepared and analysed by Raman analysis, nanoindentation, energy dispersive X-ray analysis (EDX) and atomic force microscopy (AFM). The material formed is not soft and graphitic, but of intermediate hardness (6–13 GPa) and with Raman spectral features similar to those of hydrogenated amorphous carbon, although it contains a significant Ga content (up to 25 at. %). This study was used to form sharp AFM supertip structures which were used to image sintered ceramic samples and films of aligned carbon nanotubes. Compared to traditional Si tips, this gave an improved rendering of the sample's aspect ratio although the resolution is limited by the diameter of the C supertips.

PACS 81.05.Uw; 81.07.-b; 78.30.-j

1 Introduction

The structuring and etching of carbon materials is essential for a number of applications which include field emission displays, micro-mechanical systems and data storage components [1]. The traditional method is to sequentially deposit and pattern the various components of the device. The difficulty is that both tasks often use energetic ions and electrons. For instance, diamond-like carbon (DLC), mostly prepared by plasma deposition techniques, is formed by the bombardment of energetic ionic species. A similar situation can exist for carbon nanotubes (CNT), in particular, for tubes prepared in plasma enhanced chemical vapour deposition processes, where the ions can strike with 200 eV of self-bias energy [2]. This would suggest that an optimised deposition process could well result in a pattern of transformed material with inadequate properties. For carbon, the main problem is graphitisation which for instance, is known to occur in diamond-like carbon (DLC) following intense visible [3] or ionic irradiation [4]. Ion beams are also used for doping CNT and, likewise have the potential to create defects on the surface of the CNT. Another problem with this dual deposition/patterning approach is the complexity and cost of the systems, which cannot always be justified in a commercial context. The alternative strategy discussed here is to use a single step process to simultaneously deposit and pattern the device. Its added advantage is that three-dimensional structures can easily be built by this method and in theory, process parameters (current density, kV, pressure, etc.) can be tuned more independently than in conventional plasma deposition systems.

The idea behind this technology is that hydrocarbon layers often built up on material surfaces when subjected to electron or ion beam irradiation in the presence of oil vapours from the vacuum system. Electron microscopists have always endeavoured to remove these contamination layers and observe the pristine surface below. However, over the last twenty years, there has been some effort to use this process as a writing tool for device fabrications [5]. This method has produced single electron transistors, AFM supertips and tough nm thick resist for the electrochemical formation of porous silicon [6–8]. In a preliminary study, we compared results obtained with a conventional scanning electron microscope (SEM) and a focused ion beam (FIB) system equipped with a naphthalene gas injector [9]. The work presented here discusses carbon films prepared using the same FIB-SEM dual system.

2 Experimental

We used a Quanta 3D FEI dual FIB/SEM system. The base pressure was 10^{-6} Torr and the carbon was grown from a naphthalene gas injector over $10 \times 10\,\mu m^2$ areas, using the patterning software of the instrument. The films were grown on Si wafers placed at the coincidence point of the two beams, corresponding to a 15 mm SEM working distance. The electron beam deposited (EBD) carbon structures were prepared at 1, 2 and 5 kV with current varying from 1.3 nA to 1.6 nA. The ion beam deposited (IBD) carbon structures were grown accelerating the ion beam at 30 kV with gallium ion current varying from 30 pA to 7 nA. The exposure time was fixed to give the same film thickness for all samples, according to the instrument's patterning software. The resulting approximate charge doses were 10^{-8} C/μm^2 and 10^{-9} C/μm^2 for the EBD and IBD experiments, respectively.

✉ Fax: +44-028-90366863, E-mail: p.lemoine@ulster.ac.uk

The roughness and thickness of these carbon nanostructures were analysed with a Dimension 3100 AFM microscope operating either in tapping mode or contact mode. In addition, lateral force microscopy (LFM) images were also acquired. The Raman spectra were obtained with HeNe laser excitation (633 nm) using a Labram confocal Raman microscope. The hardness (H) and Young modulus (E) of the samples were measured with a MTS nanoindenter XP®, using the dynamical contact module in continuous stiffness measurement mode. These indentations were carried out at a constant strain rate of $0.05\,s^{-1}$ up to a depth of 300 nm. The tip area function was calibrated using fused silica and the data were analysed using the Oliver and Pharr method [10]. The EDX spectra were obtained using an Oxford Instrument spectrometer coupled to a Hitachi S3200N SEM microscope operated at 5 kV, to maximize surface sensitivity. The elements C, O, Si and Ga were calibrated, respectively with graphite, quartz, Si and GaAs standard spectra acquired also at 5 kV. The quantification and calibration of the spectra were done using the Si wafer and a ZAF protocol.

3 Results

Figures 1 and 2 show the growth rate of the EBD and IBD samples, as a function of deposition parameters. The EBD growth rate decreases with SEM accelerating voltage whereas the IBD growth rate increases with the FIB current. Moreover the EBD growth rates are much smaller than the IBD ones.

The roughness R_a values of the EBD and IBD samples are, respectively 0.6 ± 0.2 nm and 3 ± 1 nm. The EBD and IBD film's thickness vary, respectively from 13 nm to 35 nm and from 350 nm to 650 nm. This indicates that the patterning software of the instrument is not accurately calibrated against growth rate. Figure 3 shows LFM images acquired at a 90° scan angle with a 0.06 N/m Si_3N_4 contact AFM probe for a milled Si area, at 0.1 nA and for an IBD carbon area also prepared at 0.1 nA. The friction signal is clearly noticeable and significantly larger than the noise signal due to cross-talk between the bending and torsion signals of the AFM photodetector. This friction contrast with respect to the unexposed area is $-0.11\,V \pm 0.01\,V$ and $0.083\,V \pm 0.01\,V$, respectively for the milled Si and IBD films. Therefore, if the FIB irradiation reduces the friction of the AFM tip on the Si substrate, it tends to increase the friction on the IBD carbon films. Moreover, we found that the friction signal does not vary significantly with the FIB current.

Some EDX spectra are shown in Fig. 4. After quantification, the EDX analysis of the IBD samples shows that these

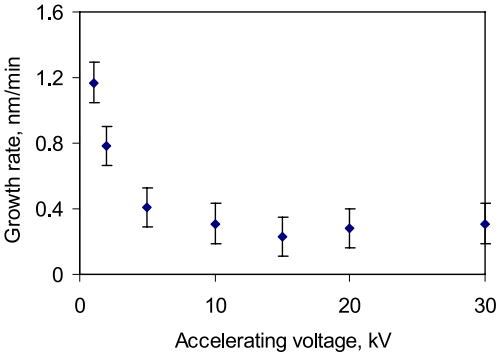

FIGURE 1 Growth rate for the EBD carbon films

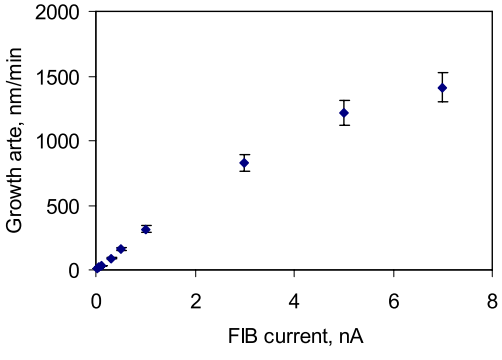

FIGURE 2 Growth rate for the IBD carbon films

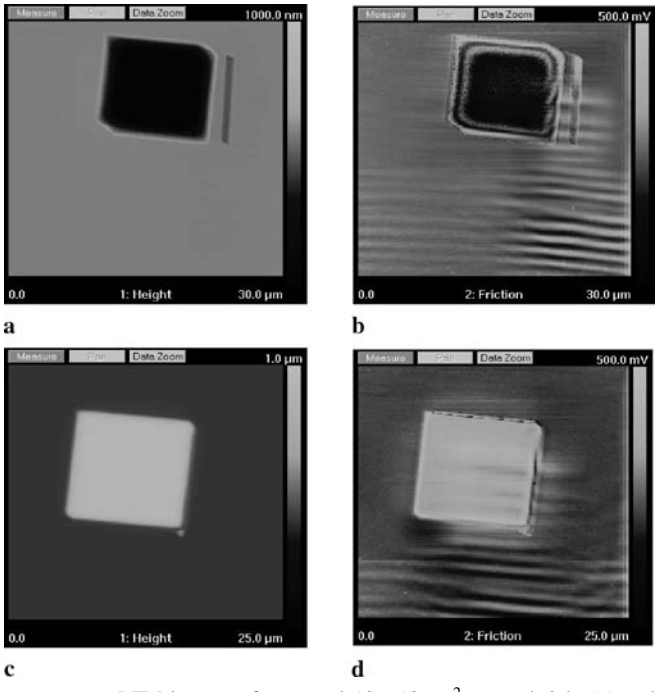

FIGURE 3 LFM images of patterned $10 \times 10\,\mu m^2$ areas; height (**a**) and friction contrast (**b**) for a milled Si at 0.1 nA and height (**c**) and friction contrast (**d**) for a IBD carbon film at 0.1 nA

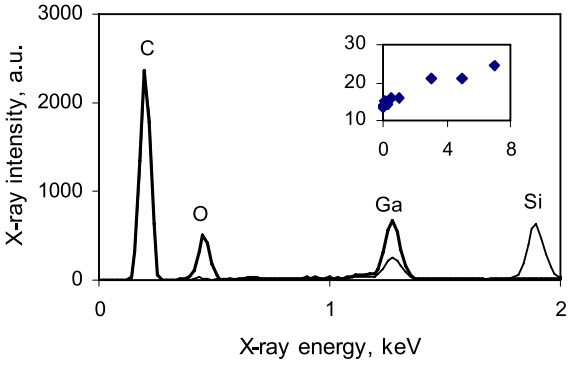

FIGURE 4 EDX spectra of an IBD film, prepared at 7 nA and a milled Si surface. The *insert* shows the Ga at.% of the various IBD films versus FIB current, in nA

films contain mainly C (75–85 at. %) and Ga (15–25 at. %), with minute quantities of O and Si (< 1 at. %), possibly originating from the substrate. The insert in Fig. 4 shows a substantial Ga atomic percentage which increases with the ion current.

Figures 5 and 6 display the Raman spectra of these EBD and IBD films. Both set of spectra show the broad asymmetric features indicative of amorphous carbon. These were deconvoluted into the usual G and D peaks, respectively around $1350\,\mathrm{cm}^{-1}$ and $1550\,\mathrm{cm}^{-1}$. The resulting G peak position and intensity ratio I_D/I_G are presented in Fig. 7 for the IBD samples.

AFM microscopy was used to locate the indents and insure that only those indents positioned on the EBD and IBD $10 \times 10\,\mu\mathrm{m}^2$ patterns were considered. In Fig. 8, we report the E and H values of the IBD samples, calculated at 10% of the film thickness ($t/10$). Although this protocol is not always valid, as the response of a coated system is influenced by the mechanical properties of the substrate [11], we expect it to be adequate in this case as the film and substrate have similar properties and the $t/10$ depth is out of the tip blunting region. The trend of the E and H values with FIB current is similar to that of the Raman parameters; a minimum is observed around 3–5 nA.

The E and H curves of the thinner EBD films were analysed using an analytical equation adapted from that of Bhattacharya taking into account tip blunting. This recently developed model, which will be published shortly, extracts the film's intrinsic hardness and Young modulus values, H_F and E_F. These H_F and E_F values for the 1 kV, 2 kV and 5 kV EBD films are, respectively, $12.9\,\mathrm{GPa} \pm 1\,\mathrm{GPa}$ and $109\,\mathrm{GPa} \pm 10\,\mathrm{GPa}$, $12.7\,\mathrm{GPa} \pm 1\,\mathrm{GPa}$ and $95\,\mathrm{GPa} \pm 10\,\mathrm{GPa}$ and $12.7\,\mathrm{GPa} \pm 1\,\mathrm{GPa}$ and $100\,\mathrm{GPa} \pm 10\,\mathrm{GPa}$.

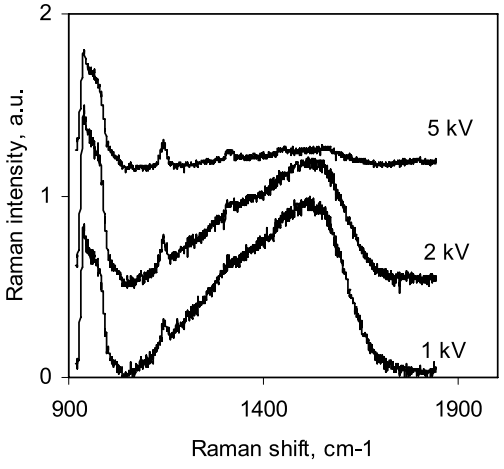

FIGURE 5 Raman spectra of the EBD samples

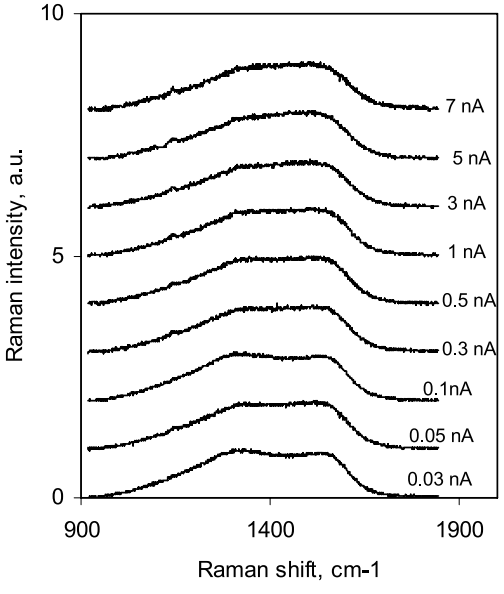

FIGURE 6 Raman spectra of the IBD samples

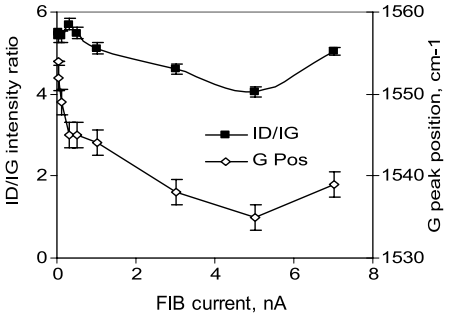

FIGURE 7 Raman intensity ratio (I_D/I_G) and G peak position (G pos.) for the IBD samples

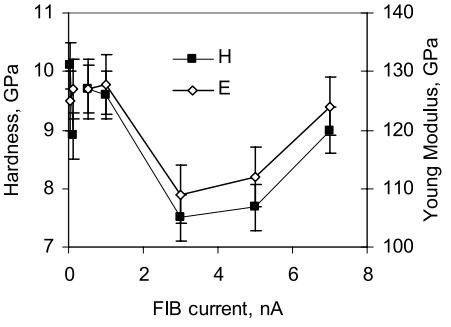

FIGURE 8 E and H values for the IBD samples at 10% of the film's thickness (50–60 nm depth)

4 Discussion

Both the EBD and IBD deposition processes rely on the generation of secondary electrons on the specimen surface, as these low energy species are the precursors which take part in the abstraction of radical and ionic species present in the ambient. In this study, we found that low accelerating voltages give higher EBD growth rates. Others observed a similar effect [12]. This is believed to be due to the decreasing secondary electron yield at higher voltages [13]. In addition, despite being exposed to higher charge doses, the EBD samples display smaller growth rates. Ohya [14] has presented comprehensive Monte Carlo simulations of the ion and electron irradiations of solids. According to this study, the generation of secondary electrons in Si is more efficient with the electron beam than with the ion beam whereas in carbon, more secondary electrons are emitted by the ion beam. As most of the growth is taking place on a carbon surface, this may explain the higher IBD growth rates.

The EDX data obtained at 5 kV indicates large Ga atomic percentages (up to 25%). The Kanaya range for 5 kV electrons is around 500 nm [15], hence these EDX analysis of the IBD samples is mostly confined to the carbon film. Again, according to Monte Carlo simulations [14], the Ga^+ ion penetrates about 10–15 nm into an aluminium target. As Si and Al have similar atomic number, we also expect the Ga to be contained within a thin surface layer, hence the Ga concentration in the surface could be much larger. Indeed Auger analysis of FIB-treated tetrahedral amorphous carbon films (t-aC) show Ga concentration up to 43 at. % in a 5 nm deep layer [16]. One can only speculate on the state or phase of gallium in these carbon films. Gallium does not wet carbon [17]. This means that carbon nanotubes [18] or microtubes [17] can be filled with gallium for thermometric applications. In another study, gallium-containing carbon deposits were found to consist of metallic gallium particulates surrounded by graphite skin layers [19]. It seems therefore that these two elements naturally segregate and, to the best of our knowledge, no structural or bonding studies have shown the presence of a gallium carbide phase. Therefore it would seem that the material implanted in our IBD films is likely to be metallic gallium. The high friction signal (Fig. 3) measured on those IBD carbon films, when compared to Si, may be due to the formation of GaN by cold welding while performing LFM imaging of these samples with the Si_3N_4 AFM tip.

The broad and asymmetric Raman features observed in this study are indicative of amorphous carbon. Considering the hydrocarbon precursor (naphthalene) and previous work done elsewhere [8], these films are probably hydrogenated. Indeed, in a previous study [9], where similar IBD carbon samples were analysed by Raman analysis at 514 nm, we did find a significant luminescence slope. This is not a direct measurement of hydrogen content but is generally accepted as evidence of hydrogen in DLC [9]. The measured E and H values suggest that these films are somewhat softer than a-C:H films prepared by conventional plasma deposition techniques, although they are much harder than purely graphitic materials such as glassy carbon and graphite (< 1 GPa). The Raman analysis of the EBD films suggests that, as the kV increases from 1 kV to 5 kV, these films become less graphitic (larger I_D/I_G ratio and higher G peak position). This has been observed by others [12]. Figures 5–7 indicate that there are more and/or larger sp^2 clusters in the IBD samples. Indeed, FIB irradiation is known to increase the sp^2 fraction of tetrahedral amorphous carbon [16] and, as EBID has been used to form ultrathin electrochemical resist [8], it is probable that the EBD material has some significant sp^3 content. However, in these hydrogenated amorphous carbon (a-C:H) films an increase in sp^3 fraction does not necessarily correspond to a mechanical strengthening of the carbon network. The Raman analysis of the IBD samples indicates that, as the FIB current increases, the sp^2 content passes through a minimum, which also correspond to a minimum of the E and H values. Studies of a-C:H films prepared by conventional plasma techniques show that dehydrogenation, and hardening can be associated with an increase in the concentration of carbon double bonds [20, 21]. In the case of these IBD samples, it may be that the implanted gallium further densifies ($\varrho_{Ga} = 5.9\,g/cm^3$) and strengthen the carbon layer.

An obvious use of these carbon nanostructures is, first of all, to produce tough AFM supertips. These were prepared in spot analysis mode at the apex of a Si AFM probe with a nominal 10 nm radius (Veeco TESP probe) using the ion beam. A first example is shown in Fig. 9a. This structure was produced with a two-stage FIB process. The large base, grown at 10 pA current, culminates in a sharper supertip needle, grown at 1 pA, 400 nm long with a sub-50 nm end radius. Figure 9b shows a tapping mode AFM image of a sintered ceramic obtained with this modified AFM tip. SEM micrographs of the AFM tip after prolonged AFM imaging periods (1 h) show that the carbon needle structure stayed intact and, therefore, is relatively tough. Another potential benefit of these C AFM supertips is their small apex angle, when compared to conventional AFM tips. This would help image high aspect ratio surfaces.

Using a longer exposure time, we prepared a second IBD supertip, approximately 2 μm long with a 100 nm tip radius. EDX mapping at low kV clearly shows that the supertip is composed of C and Ga. EDX spot analysis gives spectra which are very similar to those presented in Fig. 4. This tip was used to AFM image a square array of carbon nanotubes (CNT). SEM micrographs of that sample show diameter, length and spacing of, respectively 80 nm, 2000 nm and 500 nm. These samples are particularly difficult to image by AFM microscopy for the following reason. Taking a Young modulus of 1 TPa for the carbon nanotubes [22], we obtain a tube's stiffness $k = 0.147 \times E \times D^4/L^3 \sim 0.75$ N/m. This is hence a very compliant sample when compared to the stiffness of the TAFM lever (~ 40 N/m). Moreover the high aspect ratio of the nanotube add to the difficulty. We present in Fig. 10 a TAFM image of the sample obtained with a conventional AFM Si tip. The large apex angle of this probe tip, shown in fig. 10 b gives rise to the triangular and asymmetric cross-section (Fig. 10c), schematically interpreted in Fig. 10d.

The TAFM image of the same CNT sample obtained with the IBD C supertip is shown in Fig. 11a. In term of aspect ratio rendering, this is a better image, here the tip more accurately follows the sample surface. The AFM cross-section (Fig. 11c) also shows a more symmetrical restitution of the surface profile. However, an obvious limitation is the diameter of the supertip which alters the resolution of the AFM image.

Others have used an EBD carbon tip to observe high aspect ratio surfaces by STM [23] and AFM [24–26] imaging but, to

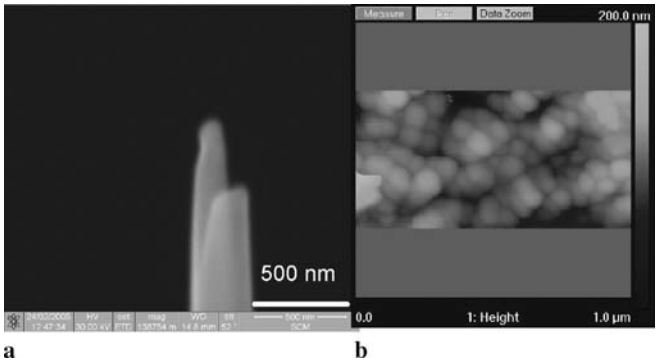

a b

FIGURE 9 SEM image of the first IBD carbon AFM supertip (**a**) and corresponding 1 μm scan TAFM image (**b**) of a sintered ceramic sample

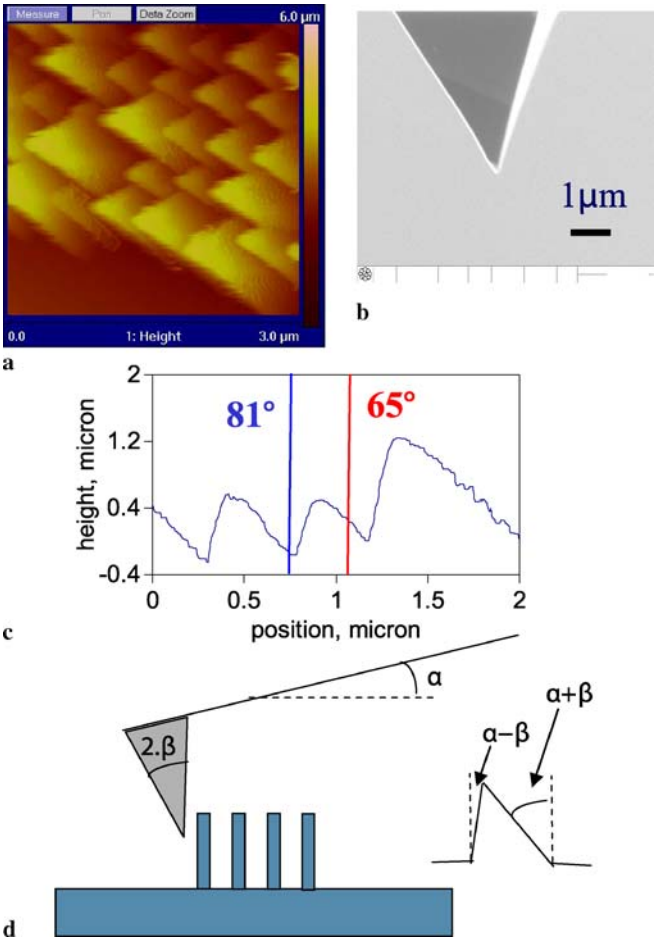

FIGURE 10 3 µm TAFM image of a CNT array using a conventional Si tip (**a**), SEM micrograph of the Si tip (**b**), AFM cross-section of the CNT sample (**c**) and schematic of the AFM reading process (**d**)

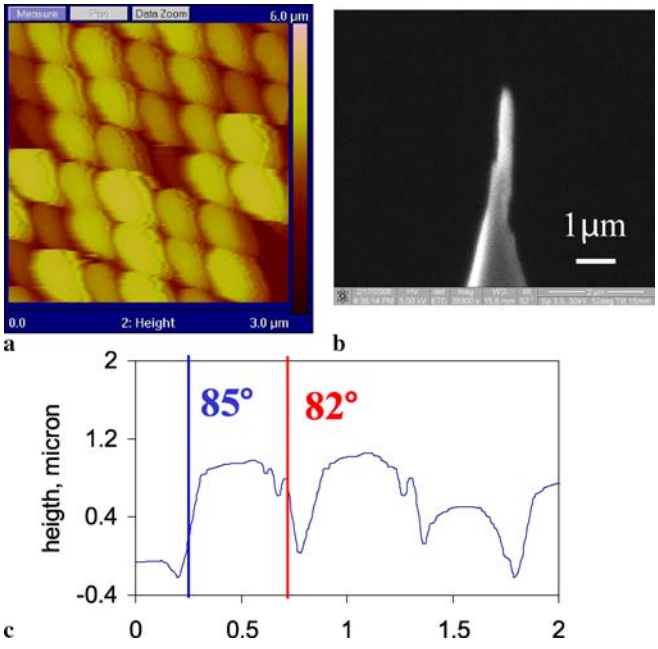

FIGURE 11 3 µm TAFM image of a CNT array using the second IBD carbon supertip (**a**), SEM micrograph of the supertip (**b**) and AFM cross-section of the CNT sample (**c**)

the best of our knowledge, this is the first time that the IBD method has been used to AFM image aligned CNT on silicon. Indeed, for the reasons stated above, to obtain AFM images of vertically oriented CNT is a challenging task and only a handful of studies have been published, [27–29]. In most cases, the aspect ratio of the tip seems to be an issue as the imaged CNT appear as conical structures. The results presented here indicate that this problem can be partially solved using the IBD technique to produce C supertips. Obviously, there are still resolution issues which need to be addressed by producing finer C supertips. The ultimate lateral resolution of the IBD or EBD deposition process depends on both the imaging performance of the system and the surface diffusion of secondary electrons [30]. It is the latter effect which represents the main limiting factor as, for both instruments; the optimised imaging spot size has a sub-10 nm diameter.

5 Conclusion

We have prepared EBD and IBD carbon films using a dual FIB/SEM system and analysed their properties by AFM, EDX, Raman and nanoindentation analysis. The films are not soft graphitic carbon but consist of an amorphous carbon of intermediate hardness (6–13 GPa), probably hydrogenated. When compared to the EBD films, the IBD samples are Ga implanted, show faster growth rates and larger graphitic content. This study permitted the forming of high aspect ratio carbon AFM supertips which were subsequently used for tapping mode AFM imaging of ceramic thin films and vertically oriented CNT samples. The supertip diameter limits the resolution of the image but allow a greater aspect ratio rendering when compared to traditional Si tips.

REFERENCES

1 Y.R. Cho, Y.R. Lee, Y.H. Song, S.Y. Kang, C.S. Hwang, M.Y. Jung, D.H. Kim, S.K. Lee, H.S. Uhm, K.I. Cho, Mater. Sci. Eng. B **79**, 128 (2001)
2 A.V. Melechko, V.I. Nerkulov, T.E. McKnight, M.A. Guillorn, K.L. Klein, D.H. Lowndes, M.L. Simpson, Appl. Phys. Rev. **97**, 41 301 (2005)
3 R.W. Lamberton, S.M. Morley, P.D. Maguire, J.A. McLaughlin, Thin Solid Films **333**, 114 (1998)
4 N.A. Marks, J.M. Bell, G.K. Pearce, D.R. McKenzie, M.M.M. Bilek, Diam. Relat. Mater. **12**, 2003 (2003)
5 J. Taniguch, I. Miyamoto, N. Ohno, S. Honda, Nucl. Instrum. Methods Phys. Res. B **121**, 507 (1997)
6 M. Komuro, H. Hiroshima, Microelectron. Eng. **35**, 273 (1997)
7 M. Castagne, M. Benfedda, S. Lahimer, P. Falgayrettes, J.P. Fillard, Ultramicroscopy **76**, 187 (1999)
8 T. Djenizian, L. Santinacci, H. Hildebrand P. Schmuki, Surf. Sci. **524**, 40 (2003)
9 P. Lemoine, J.P. Quinn, P.P. Papakonstantinou, P.D. Maguire, J.A. McLaughlin, *Improved Carbon Materials for Nano-manufacturing Applications*, in: *CRC Handbook of Nanomanufacturing*, ed. by A. Bushnaina (Taylor and Francis, New York, 2006)
10 W.C. Oliver, G.M. Pharr, J. Mater. Res. **7**, 1564 (1992)
11 A.K. Bhattacharya, W.D. Nix, Int. J. Solid Struct. **24**, 1287 (1988)
12 W. Ding, D.A. Dikin, X. Chen, R.D. Piner, R.S. Ruoff, E. Zussman, X. Wang, X. Li, J. Appl. Phys. **98**, 14 905 (2005)
13 M. Amman, J.W. Sleight, D.R. Lombardi, R.E. Welser, M.R. Despande, M.A. Reed, L.J. Guido, J. Vac. Sci. Technol. B **14**, 54 (1996)
14 K. Ohya, T. Ishitani, Nucl. Instrum. Methods Phys. Res. B **202**, 305 (2003)
15 P. Lemoine, R.W. Lamberton, A.A. Ogwu, J.F. Zhao, P. Maguire, J. McLaughlin, J. Appl. Phys. **86**, 6564 (1999)

16 A. Stanishevsky, L. Khriachtchev, J. Appl. Phys. **86**, 7052 (1999)
17 G. Bhimarasetti, J.M. Cowley, M. K Sunkara, Nanotechnology **16**, S362 (2005)
18 Y. Gao, Y. Bando, Nature **415**, 599 (2002)
19 C. Park, J.H. Kim, D. Yoon, S. Han, C. Doh, S. Yeo, K.H. Lee, T.J. Andersonc, J. Electrochem. Soc. **152**, 298 (2005)
20 W. Jakob, Thin Solid Films **326**, 1 (1998)
21 P. Lemoine, J.P. Quinn, P.D. Maguire, P.P. Papakonstantinou, N. Dougan, Thin Solid Films **514**, 223 (2006)
22 J.P. Salvetat, J.M. Onard, N.H. Thomson, A.J. Kulik, L. Forro, W. Benoit, L. Zuppiroli, Appl. Phys. A **69**, 255 (1999)
23 Y. Akama, E. Mishimura, A. Sakai, H. Murakami, J. Vac. Sci. Technol. A **8**, 429 (1990)
24 M. Wendel, H. Lorenz, J.P. Kotthaus, Appl. Phys. Lett. **67**, 3732 (1995)
25 M. Yamaki, T. Miwa, H. Yoshimura, K. Nagayama, J. Vac. Sci. Technol. B **10**, 2447 (1992)
26 F. Zenhausern, M. Adrian, B. ten Heggeler-Bordier, F. Ardizzoni, P. Descouts, J. Appl. Phys. **73**, 7232 (1993)
27 H.Y. Yap, B. Ramaker, A.V. Sumant, R.W. Carpick, Diam. Relat. Mater. **15**, 1622 (2006)
28 B. Kim, W.M. Sigmund, Colloid Surf. A: Physicochem. Eng. Aspects **266**, 91 (2005)
29 X. Nan, Z. Gu, Z. Liu, J. Colloid Interf. Sci. **245**, 311 (2002)
30 N. Silvis-Cividjian, C.W. Hagen, L.H.A. Leunissen, P. Kruit, Microelectron. Eng. **61**–**62**, 693 (2002)